PCCP

ROYAL SOCIETY OF CHEMISTRY

PAPER

View Article Online
View Journal | View Issue

Check for updates

Cite this: *Phys. Chem. Chem. Phys.*, 2024, **26**, 3197

Activation of H_2 using *ansa*-aminoboranes: solvent effects, dynamics, and spin hyperpolarization†

Karolina Konsewicz,‡[a] Gergely Laczkó,‡[bc] Imre Pápai [b] and Vladimir V. Zhivonitko *[a]

Spin hyperpolarization generated upon activation of parahydrogen, the spin-0 isomer of H_2, by *ansa*-aminoboranes (AABs) constitutes a rare but interesting example of applied metal-free catalysis in parahydrogen-induced polarization (PHIP). AAB molecular moieties made of light elements would be useful in important areas of NMR, such as chemosensing and the production of hyperpolarized substances, or generally in NMR sensitivity enhancement. At the same time, little is known about the detailed mechanistic aspects of underlying chemical processes. Herein, we present a joint experimental-computational study of the kinetic and thermodynamic aspects of H_2 activation by AABs, for the first time providing molecular-level details and results of PHIP experiments with AABs in various solvents. Specifically, a large number of kinetic and thermodynamic parameters are measured experimentally for H_2 activation by 2-aminophenylboranes of variable steric bulkiness of the boryl site. A clear correlation between the experimental and DFT-predicted thermochemical parameters is observed. PHIP effects in toluene, dichloromethane, and acetonitrile are characterized and rationalized based on the use of the kinetic and nuclear spin relaxation parameters. Altogether, the obtained results provide valuable information for the further rational design of efficient AAB catalysts for metal-free PHIP based on frustrated Lewis pair (FLP) chemistry.

Received 29th November 2023,
Accepted 21st December 2023

DOI: 10.1039/d3cp05816f

rsc.li/pccp

Open Access Article. Published on 22 December 2023. Downloaded on 5/7/2026 11:03:45 AM.
This article is licensed under a Creative Commons Attribution 3.0 Unported Licence.

1. Introduction

The metal-free activation of small molecules has garnered considerable attention due to its potential for the development of new catalysts based on abundant main group elements.[1,2] In addition, it can likely be utilized in the design of chemosensors that are sensitive to small molecules. For instance, metal-free *ansa*-aminoboranes that can activate molecular hydrogen were shown to activate parahydrogen, the spin-0 isomer of H_2, which leads to strongly enhanced signals in ^{1}H NMR spectra (Scheme 1).[3,4] With *ortho*-phenylene-based *ansa*-aminoboranes, spontaneous ^{15}N and ^{11}B hyperpolarization using parahydrogen was also demonstrated,[5] potentially opening the possibility of background-free NMR chemosensing of parahydrogen utilizing these species. Moreover, *ansa*-aminoboranes **CAT**, **QCAT** and **HCAT** (Scheme 1) were shown to act as efficient catalysts in the hydrogenation of alkynes and imines leading to hyperpolarized alkenes and amines, respectively.[6,7] To a certain extent, this class of catalytic materials can be considered as a more

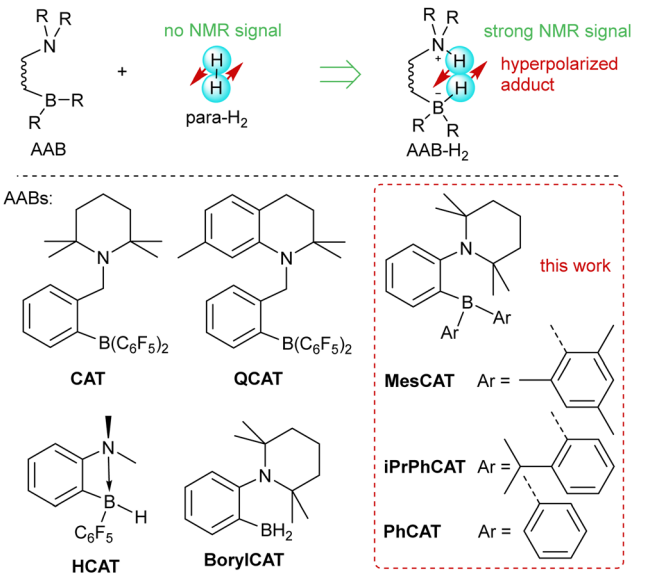

Scheme 1 Activation of parahydrogen by *ansa*-aminoboranes (AABs).

[a] *NMR Research Unit, Faculty of Science, University of Oulu, P.O. Box 3000, Oulu, 90014, Finland. E-mail: vladimir.zhivonitko@oulu.fi*
[b] *Institute of Organic Chemistry, Research Centre for Natural Sciences, Magyar Tudósok Körútja 2, H-1117 Budapest, Hungary*
[c] *Hevesy György PhD School of Chemistry, Eötvös Loránd University, P.O. Box 32, H-1518 Budapest, Hungary*

† Electronic supplementary information (ESI) available: Description of experiments; theory and computations; animation of H_2 activation. See DOI: https://doi.org/10.1039/d3cp05816f

‡ Both authors contributed equally to this manuscript.

Open Access Article. Published on 22 December 2023. Downloaded on 5/7/2026 11:03:45 AM.
This article is licensed under a Creative Commons Attribution 3.0 Unported Licence.

sustainable and environmentally friendly alternative to transition metal catalysts usually employed in parahydrogen-based spin hyperpolarization techniques.[8]

Understanding the mechanism of H_2 activation by *ansa*-aminoboranes on both macroscopic and microscopic levels can provide detailed insights into the molecular features facilitating the activation process. This can be used in the design of new *ansa*-aminoboranes with desired kinetic and thermodynamic properties, dramatically increasing the nuclear spin hyperpolarization efficiency. It is worth noting that other metal-free compounds such as triphosphabenzene[9] and pnictogen biradicals[10,11] and tetraradicals[12] have also been documented to exhibit hyperpolarization effects with parahydrogen. However, we believe that *ansa*-aminoboranes provide the most versatile metal-free scaffold for parahydrogen activation. It is worth noting that the intramolecular nature of *ansa*-aminoboranes is crucial for the observation of parahydrogen-induced polarization (PHIP), since attempts to use intermolecular FLPs did not reveal any hyperpolarization effects.[7] However, the solvent effects on H_2 activation using these interesting compounds in conjunction with PHIP have never been studied.

In the realm of catalytic research, PHIP is a particularly valuable nuclear spin hyperpolarization technique due to the fact that hyperpolarization transpires organically when H_2 molecules enriched in the para nuclear spin isomer are chemically activated.[13,14] Mechanistic insights can be obtained by observing the significantly amplified NMR signals of the reaction intermediates or final products when a catalyst is used to activate parahydrogen. To see the hyperpolarization, it is necessary for H_2 activation to be pairwise, implying that the H atom pair must not be completely separated, at least during the initial parahydrogen activation phase.[8] In particular, the ability of PHIP to identify dihydride intermediates has been illustrated through its application in elucidating the hydrogenation mechanisms of numerous metal complex catalysts.[8,15] As intriguing examples, the kinetics of the formation of $[IrCO(H)_2I(PPh_3)_2]$ subsequent to the reductive elimination of hydrogen induced by light was investigated using parahydrogen,[16] cationic RhI intermediates with coordinated arene rings were detected;[17] the pathways of H_2 exchange in $(\mu\text{-}H)_2Os_3(CO)_{10}$ clusters were determined;[18] ligand exchange in $[IrCO(H)_2Cl(PPh_3)_2]$ and $[IrH_2Cl(PPh_3)_3]$ was understood;[19] and many other important mechanistic studies[8,15,20] were done, including also those of heterogeneous catalytic systems.[21,22]

In this paper, we discuss for the first time the key factors influencing the activation of molecular hydrogen by a selection of PHIP-relevant ortho-phenylene *ansa*-aminoboranes in various solvents. These factors are crucial for the observation of PHIP in general. We report a significant amount of experimentally measured kinetic and thermodynamic data for **MesCAT**, **iPrPhCAT**, and **PhCAT** *ansa*-aminoboranes (Scheme 1), model species with variable steric bulkiness at the boron center. We describe the observed parameters based on DFT calculations, showing that the applied computational approach can be used to predict these parameters with good accuracy. Both experiments and computations show a stabilization effect of the *ansa*-aminoborane-H_2 adduct in polar solvents. Altogether, kinetic, thermodynamic, relaxation, and computational data are used to rationalize the observed nuclear spin hyperpolarization effects observed in activation parahydrogen using the studied *ansa*-aminoboranes in toluene, dichloromethane, and acetonitrile as representative solvents of variable polarity that do not interact with the FLP centers.

2. Methods

2.1 Chemicals and materials

Ansa-Aminoborane compounds were synthesized according to the previously described methods.[4,5] All the required chemicals were purchased from commercial sources. Deuterated solvents were dried under molecular sieves (3 Å). Parahydrogen-enriched H_2 gas (92%), referred to simply as ''parahydrogen'' in the following discussion, was produced using a Bruker parahydrogen generator.

2.2 Parahydrogen experiments

PHIP NMR experiments were performed on a Bruker AV 400 NMR spectrometer operating at 400 MHz ^{1}H resonance frequency and equipped with a broad-band 5 mm RF probe. A standard temperature control unit of the instrument was used to maintain the desired sample temperature.

In a typical experiment, a 5 mm sample tube (Wilmad) containing a *ca.* 0.05 M solution of ^{15}N-labeled *ansa*-aminoboranes **MesCAT**, **iPrPhCAT**, or **PhCAT** in degassed dry toluene-d_6 or acetonitrile-d_3 was placed inside the NMR magnet, and parahydrogen was bubbled through the solution for 10 s. Then the parahydrogen flow was abruptly switched off, and an ^{1}H NMR experiment using $\pi/4$-pulse was started. ^{11}B decoupling (WALTZ16) was used for the acquisitions. Parahydrogen was supplied to the bottom of the sample tube through 1/32″ PTFE tubing under a pressure of 5 bar. The enhancement factors were determined by comparing the integral amplitudes of individual components of the enhanced ^{1}H NMR antiphase doublets to those in the thermal spectrum.

2.3 Kinetic and thermodynamic measurements

Measurements of kinetic rate constants were performed using the spin saturation transfer method[23–25] on a Bruker Avance III 600 MHz spectrometer, similarly to those described in ref. 4. A valved 5 mm NMR tube from Wilmad was used in the experiments. The samples were prepared by charging the tube with AAB solutions ($\sim$0.05 M) and 5 bars of normal (thermal) H_2. ^{15}N decoupling (WALTZ16) was used for all acquisitions. The thermally polarized NH group proton signals were used to determine the rate constants for the dissociation of AAB-H_2 adducts into AAB and H_2 (k_{dis}, see eqn (1) in Section 3.1). The constants were calculated from the ratios of the signals in the normal spectra and in the spectra acquired with presaturation of the ortho-H_2 resonance at *ca.* 4.6 ppm. To determine k_{dis}, the following expression was used: $k_{dis} = (S_n/S_s - 1)/T_1^{NH}$, in which S_n is the signal intensity in the normal spectrum, S_s is the signal intensity in the spectrum with saturation, and T_1^{NH} is the

 This journal is © the Owner Societies 2024

Open Access Article. Published on 22 December 2023. Downloaded on 5/7/2026 11:03:45 AM. This article is licensed under a Creative Commons Attribution 3.0 Unported Licence.

relaxation time of the proton in the NH group. The saturation-recovery protocol with irradiation of H_2 resonance during the recovery delays was used to determine T_1^{NH} as described in ref. 4.

Equilibrium constants K_c (see eqn (2)) were determined using signal ratios of AAB, AAB-H_2, and H_2 in the thermal ^{1}H NMR spectra of the samples. Concentration scaling was required for the conversion from signal amplitude units to concentrations, which was done using the signal integrals and the known initial concentration of AABs. The association rate constant is derived as $k_{as} = K_c k_{dis}$. The standard enthalpies and entropies of the reaction were determined from K_c values at different temperatures using the equation of chemical reaction isotherm.

The enthalpy and entropy activation parameters for the AAB-H_2 dissociation were determined by the linear regression procedure of Eyring[26] plots. The corresponding data are shown in ESI† (Fig. S1–S6).

2.4 Computational methods

Density functional theory (DFT) was applied to identify the most stable forms of H_2 adducts of ansa-aminoboranes, the transition states of the H_2 activation process, and also to characterize the conformational changes. The ωB97X-D functional was chosen for DFT calculations, which is a dispersion-corrected, range-separated hybrid exchange–correlation functional developed by Chai and Head-Gordon.[27–29] The geometries were optimized at the ωB97X-D/6-311G** level of theory, and the thermal and entropic corrections were also estimated at this level. Single point solvation Gibbs free energies were calculated with the SMD model[30] using the gas phase structures for all relevant solvents. Electronic energies were recalculated at the more accurate ωB97X-D/6-311++G(3df,3pd) level. All calculations were carried out with the Gaussian 16 package.[31]

3. Results and discussion

In the following sections, we present and discuss the activation of H_2 by *ansa*-aminoboranes from the perspectives of chemical kinetics (Section 3.1), microscopic dynamics (Section 3.2), and spin hyperpolarization (Section 3.3) to build a reasonably full picture describing observations in parahydrogen experiments.

3.1 Kinetics and thermodynamics of H_2 activation

Formally, H_2 activation by *ansa*-aminoboranes is a second order kinetic process in the forward (association) direction and a first order process in the reverse (dissociation) direction with rate constants k_{as} and k_{dis}, respectively,

$$\mathrm{AAB} + \mathrm{H_2} \underset{k_{dis}}{\overset{k_{as}}{\rightleftharpoons}} \mathrm{AAB\text{-}H_2} \quad (1)$$

and the equilibrium constant

$$K_c = \frac{[\mathrm{AAB\text{-}H_2}]_0}{[\mathrm{AAB}]_0[\mathrm{H_2}]_0} = \frac{k_{as}}{k_{dis}}. \quad (2)$$

Both forward and reverse reaction rates play a crucial role in the observation of hyperpolarization effects because the shapes and amplitudes of signals enhanced by parahydrogen-derived hyperpolarization upon H_2 activation are strongly dependent on the reaction kinetics.[4] For instance, slow dissociation kinetics (small k_{dis}) can lead to significantly decreased hyperpolarization levels through the increased influence of spin relaxation in the resulting AX spin pair of the AAB-H_2 adducts (see Section 3.3 for details). This influence is strongly non-linear, so that very fast kinetics may also have deleterious effects for the parahydrogen experiments. Generally, kinetic parameters are sensitive to the experimental conditions, such as temperature and solvent used. Therefore, to draw an insightful interpretation of experimental observations, we first present the experimentally measured reaction rates and relaxation times in Table 1.

The experimental data reveal a strong dependence of the kinetic parameters, k_{dis} and k_{as}, as well as the equilibrium constant, K_c, on the solvent used. Specifically, the adduct dissociation constant, k_{dis}, revealed a significant dependence on the solvent polarity. For all studied *ansa*-aminoboranes, this parameter has the highest value in toluene (non-polar solvent) and the lowest value in acetonitrile (polar solvent) under otherwise similar conditions and reaction temperatures. Dichloromethane experiments provided some intermediate values, correlating with its polarity. In contrast, the association constant, k_{as}, showed much weaker solvent dependence. Together, the solvent effects stemming from the kinetics of the reversible H_2 activation affected the equilibrium constant $K_c = k_{as}/k_{dis}$, making it also solvent dependent.

The overall trend is that the higher polarity of the solvent shifts the equilibrium towards the formation of AAB-H_2 adducts. K_c values in toluene are approximately two orders of magnitude smaller than in acetonitrile, which dramatically changes the $[\mathrm{AAB\text{-}H_2}]_0/[\mathrm{AAB}]_0$ equilibrium ratio, implying that the concentration of the AAB-H_2 adduct is significantly smaller in non-polar toluene than in polar acetonitrile for a given initial concentration of *ansa*-aminoborane (see Table 1 for data).

The strong dependence of the AAB-H_2 dissociation step on the solvent is clearly visible in the analysis of standard activation Gibbs free energies $\Delta G^{\#dis}$ (298 K) derived from the experimentally measured kinetic data by using Eyring plot analysis (see Section 2.3), Table 2. The free energies of dissociation are lower by approximately 2 kcal mol^{-1} in toluene as compared to acetonitrile for all studied *ansa*-aminoboranes, implying that the energetic barrier for elimination of H_2 is significantly smaller in the non-polar solvent. The reasons for such an effect can be attributed to the stabilization/destabilization influence of solvation on either the AAB-H_2 adduct molecule or on the corresponding transition state. These details are discussed below based on the microscopic picture provided by DFT calculations. However, looking at the standard enthalpies of the overall reaction, ΔH_r, we can deduce that polar solvents lead to the clear thermal stabilization of AAB-H_2 adducts, as the use of acetonitrile leads to an enthalpic drop of at least 6 kcal mol^{-1} as compared to the toluene data. This seems to be well justified, as the adduct has a zwitterionic

Open Access Article. Published on 22 December 2023. Downloaded on 5/7/2026 11:03:45 AM.
This article is licensed under a Creative Commons Attribution 3.0 Unported Licence.

Table 1 Experimental kinetic and thermodynamic parameters of H_2 activation by the studied *ansa*-aminoboranes

AAB	Solvent	T (K)	k_{dis} (s^{-1})	k_{as} (M^{-1} s^{-1})	K_c (M^{-1})	$[AAB\text{-}H_2]_0/[AAB]_0$	$[AAB\text{-}H_2]_0/[H_2]_0$	T_1^{NH} (s)
MesCAT	tol[a]	293	1.5 ± 0.1	0.30 ± 0.04	0.20 ± 0.05	2.8×10^{-3}	6.9×10^{-3}	0.29 ± 0.03
		299	3.2 ± 0.4	0.53 ± 0.06	0.16 ± 0.03	2.3×10^{-3}	5.4×10^{-3}	0.32 ± 0.02
		304	5.3 ± 0.5	0.71 ± 0.07	0.13 ± 0.03	1.9×10^{-3}	4.1×10^{-3}	0.32 ± 0.02
	dcm[b]	283	0.02 ± 0.01	0.10 ± 0.01	5.2 ± 1.1	0.11	0.22	0.38 ± 0.04
		293	0.10 ± 0.02	0.20 ± 0.02	2.3 ± 0.4	0.05	0.10	0.42 ± 0.04
		303	0.32 ± 0.03	0.32 ± 0.04	1.0 ± 0.2	0.03	0.05	0.49 ± 0.06
	acn[a]	298	0.040 ± 0.003	0.52 ± 0.06	13.0 ± 2.2	0.22	0.05	0.55 ± 0.05
		304	0.07 ± 0.01	0.59 ± 0.05	8.6 ± 1.4	0.15	0.07	0.57 ± 0.04
		310	0.15 ± 0.01	1.0 ± 0.1	6.7 ± 1.4	0.11	0.11	0.64 ± 0.06
iPrPhCAT	tol[a]	293	0.25 ± 0.02	8.6 ± 0.9	34 ± 8	0.48	0.99	0.30 ± 0.03
		299	0.78 ± 0.09	21 ± 2	27 ± 6	0.37	0.74	0.32 ± 0.04
		304	1.58 ± 0.15	34 ± 3	22 ± 3	0.31	0.58	0.33 ± 0.04
	dcm[b]	283	0.010 ± 0.005	12 ± 1	1200 ± 270	20	1.20	0.30 ± 0.04
		293	0.040 ± 0.006	20 ± 2	462 ± 90	8	0.99	0.35 ± 0.04
		303	0.18 ± 0.02	36 ± 4	192 ± 50	4	0.80	0.42 ± 0.05
	acn[a]	319	0.17 ± 0.02	109 ± 13	643 ± 100	12	0.84	0.63 ± 0.05
		322	0.23 ± 0.02	115 ± 11	502 ± 90	10	0.75	0.64 ± 0.07
		327	0.39 ± 0.05	144 ± 12	369 ± 90	7	0.67	0.70 ± 0.05
PhCAT	tol[a]	287	17 ± 2	509 ± 50	29.6 ± 5.4	0.41	1.10	0.22 ± 0.02
		293	30 ± 3	703 ± 70	23.4 ± 5.7	0.33	0.77	0.24 ± 0.02
		299	59 ± 4	1093 ± 90	18.6 ± 4.5	0.26	0.58	0.24 ± 0.03
	dcm[b]	283	0.40 ± 0.04	840 ± 70	2110 ± 300	26	2.56	0.28 ± 0.03
		293	1.6 ± 0.1	1440 ± 170	800 ± 180	10	2.15	0.32 ± 0.03
		303	5.4 ± 0.6	1620 ± 160	320 ± 80	5	1.76	0.38 ± 0.03
	acn[a]	298	0.7 ± 0.1	600 ± 50	858 ± 170	15	1.44	0.46 ± 0.04
		310	2.2 ± 0.2	915 ± 80	415 ± 70	8	1.34	0.52 ± 0.05
		316	3.9 ± 0.4	1102 ± 80	282 ± 70	5	1.30	0.54 ± 0.06

[a] This work. [b] Taken from ref. 4.

structure that must be stabilized by the solvation effects in polar solvents.

3.2 Microscopic picture of H_2 activation

The formal kinetic and thermodynamic considerations described above give an overall picture of H_2 activation without specific mechanistic details. Microscopically, however, the activation of H_2 by *ansa*-aminoboranes has features that are useful to bear in mind for the parahydrogen experiments and are important for understanding the reaction mechanism in general. Our DFT calculations indicate that the H_2 activation occurs *via* the concerted action of Lewis acidic and basic sites of the *ansa*-aminoborane. The identified transition states reflect the general characteristics of FLP-assisted heterolytic H_2 splitting, namely the end-on $N\cdots H_2$ and side-on $H_2\cdots B$ interactions, which is consistent with the electron transfer (ET) reactivity model.[32] The corresponding reaction pathways for the studied *ansa*-aminoboranes are illustrated in the supporting animation (see ESI†). All the H_2 activation transition states have an early nature in that their

Table 2 Selected experimental thermochemical parameters of the reversible H_2 activation by *ansa*-aminoboranes

AAB	Solvent	$\Delta G^{\#dis}$ (298 K) kcal mol^{-1}	$\Delta H^{\#dis}$ kcal mol^{-1}	$\Delta S^{\#dis}$ cal mol^{-1} K^{-1}	ΔH_r kcal mol^{-1}	ΔS_r cal mol^{-1} K^{-1}
MesCAT	tol[a]	16.8	19 ± 2	6 ± 6	−7 ± 1	−28 ± 7
	dcm[b]	18.4	23 ± 8	16 ± 25	−14 ± 4	−48 ± 27
	acn[a]	19.4	22 ± 2	7 ± 8	−13 ± 2	−40 ± 15
iPrPhCAT	tol[a]	17.6	20 ± 1	8 ± 4	−10 ± 1	−27 ± 10
	dcm[b]	18.9	23 ± 1	13 ± 3	−15 ± 2	−39 ± 14
	acn[a]	19.8	19 ± 3	−2 ± 8	−16 ± 2	−38 ± 15
PhCAT	tol[a]	15.1	16 ± 1	2 ± 5	−8 ± 1	−21 ± 13
	dcm[b]	16.8	21 ± 1	15 ± 2	−17 ± 3	−44 ± 10
	acn[a]	17.7	18 ± 1	0 ± 1	−13 ± 1	−32 ± 7

[a] This work. [b] Taken from ref. 4. $\Delta G^{\#dis}$ is given for 298 K.

 This journal is © the Owner Societies 2024

Open Access Article. Published on 22 December 2023. Downloaded on 5/7/2026 11:03:45 AM.
This article is licensed under a Creative Commons Attribution 3.0 Unported Licence.

structures resemble closely to those of the corresponding AAB + H_2 states. In terms of the AAB-H_2 → AAB + H_2 dissociation processes, these transition states have a late nature, so one expects notable entropic contributions to the free energy barriers of H_2 elimination reactions. Interestingly, the measured entropic contributions reported in Table 2 are not so significant (3–5 kcal mol^{-1}).

It is noticeable that the DFT analysis revealed a clear correlation between the computed activation free energies and the experimentally observed ones presented in Table 2. Specifically, Fig. 1 shows the computed *vs.* experimental $\Delta G^{\#dis}$ (298 K) data plot for the dissociation step. The correlation is quite encouraging considering that both experimental and computational data have their intrinsic uncertainties. The uncertainty of the measurements typically ranges from 1 to 3 kcal mol^{-1}, depending on the case, and one expects similar uncertainties for the DFT predictions as well. The reasonable agreement between theory and experiment implies that the presented computational approach could be used for the estimation of the thermochemical parameters for additional structures of *ansa*-aminoboranes in future studies. Another important outcome of this comparison is that it provides support for the reaction mechanism established from computational studies, enriching the information content with fine details inaccessible by the formal kinetic approach.

The computed thermodynamic stabilities of AAB-H_2 adducts in the form for the Gibbs free energies of reaction (eqn (1)) are compiled in Table 3. The data indicate that the introduction of electron donating alkyl groups (Me or iPr) on the borane phenyl substituents reduces the thermodynamic feasibility of H_2 activation. This is likely due to electronic effects (the borane unit becomes less acidic), but steric effects may also influence the thermodynamics. The substituent effect is particularly notable for **MesCAT**. It is also apparent that the relative stability of the adduct states is fairly sensitive to the polarity of the solvent since the zwitterionic AAB-H_2 products are stabilized by more polar solvents. We note that the barrier of H_2 splitting is much less influenced by the polarity of the solvent, which can be associated with the early nature of the transition states.

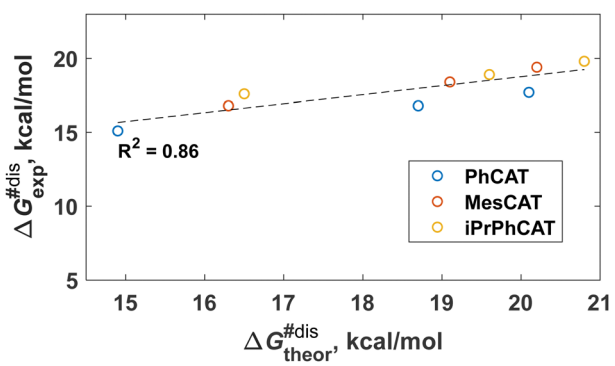

Fig. 1 A graph showing the correlation between calculated and experimentally measured standard free energies of activation for the AAB-H_2 dissociation reaction. **MesCAT**, **iPrPhCAT**, and **PhCAT** data are used to plot the graph. $\Delta G^{\#dis}$ is given for 298 K.

Table 3 Stabilities of the most stable forms of AAB-H_2 adducts in various solvents according to DFT

	ΔG_r (298 K),[a] kcal mol^{-1}		
AAB	Tol	DCM	MeCN
MesCAT-H_2	3.1	0.3	−0.8
iPrPhCAT-H_2	−0.2	−3.5	−4.2
PhCAT-H_2	−0.4	−4.2	−5.7

[a] The Gibbs free energies of reaction (eqn (1)) are given with respect to the corresponding reactant states (AAB + H_2).

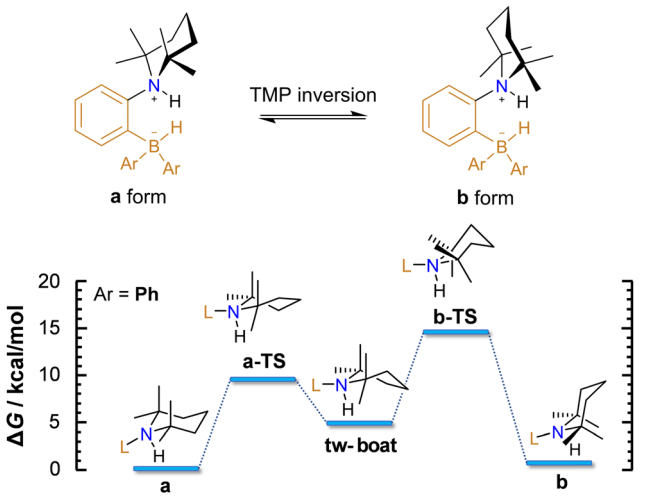

Fig. 2 Dynamic inversion of the TMP group in *ansa*-aminoboranes, wherein two stable forms, **a** and **b**, are present. As an example, an energetic diagram for TMP inversion in **PhCAT-H_2** (in DCM) is shown to illustrate the mechanism of the inversion. ΔG is given for 298 K.

At the microscopic level, the H_2 activation process is accompanied by molecular rearrangements, which will be discussed herein. Concerning the AAB-H_2 adducts of the studied *ansa*-

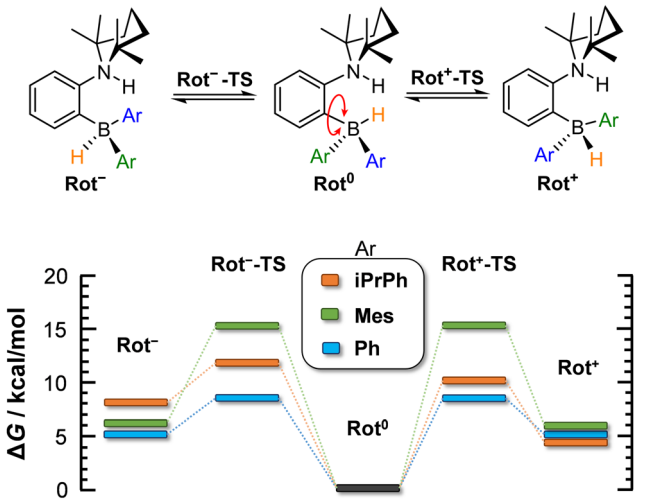

Fig. 3 Computed energetics corresponding to borohydride site rotation in AAB-H_2 adducts (in DCM). ΔG is given for 298 K.

Open Access Article. Published on 22 December 2023. Downloaded on 5/7/2026 11:03:45 AM.
This article is licensed under a Creative Commons Attribution 3.0 Unported Licence.

aminoboranes, two internal structural rearrangements are important: (1) inversion of the 2,2,6,6-tetramethylpiperidine (TMP) ring (Fig. 2) and (2) rotation of the $-BHAr_2$ unit of the adduct (Fig. 3).

According to DFT calculations, TMP inversion that interconnects the **a** and **b** forms of AAB-H_2 adducts proceeds in two steps, as exemplified in the reaction with **PhCAT** (Fig. 2). Herein, the chair structure of form **a** first transforms into a twisted boat conformer (*via* **a-TS**), which is then converted to form **b** (*via* **b-TS**). The second transition state is predicted to be higher in free energy, but the overall barrier of TMP inversion (14.0 kcal mol^{-1}) is lower than that of H_2 elimination (18.7 kcal mol^{-1}). Calculations predict the **a** and **b** forms to have similar stabilities; they differ only by 0.4 kcal mol^{-1}. These results suggest fast dynamic exchange between these two forms of AAB-H_2 adducts, so it is impossible to distinguish between them in ^{1}H NMR spectra under ambient conditions.

In contrast, the rotation of $-BHAr_2$ groups can lead to rotamers (rotated forms) that are significantly different in free energy. The rotation of the borohydride unit was investigated with all the three AABs, but only in their **a** forms. The barriers of the rotation and the stabilities of the rotamers are summarized in Fig. 3. In the most stable forms of AAB-H_2, the H atoms originating from H_2 atoms are close to each other, which is due

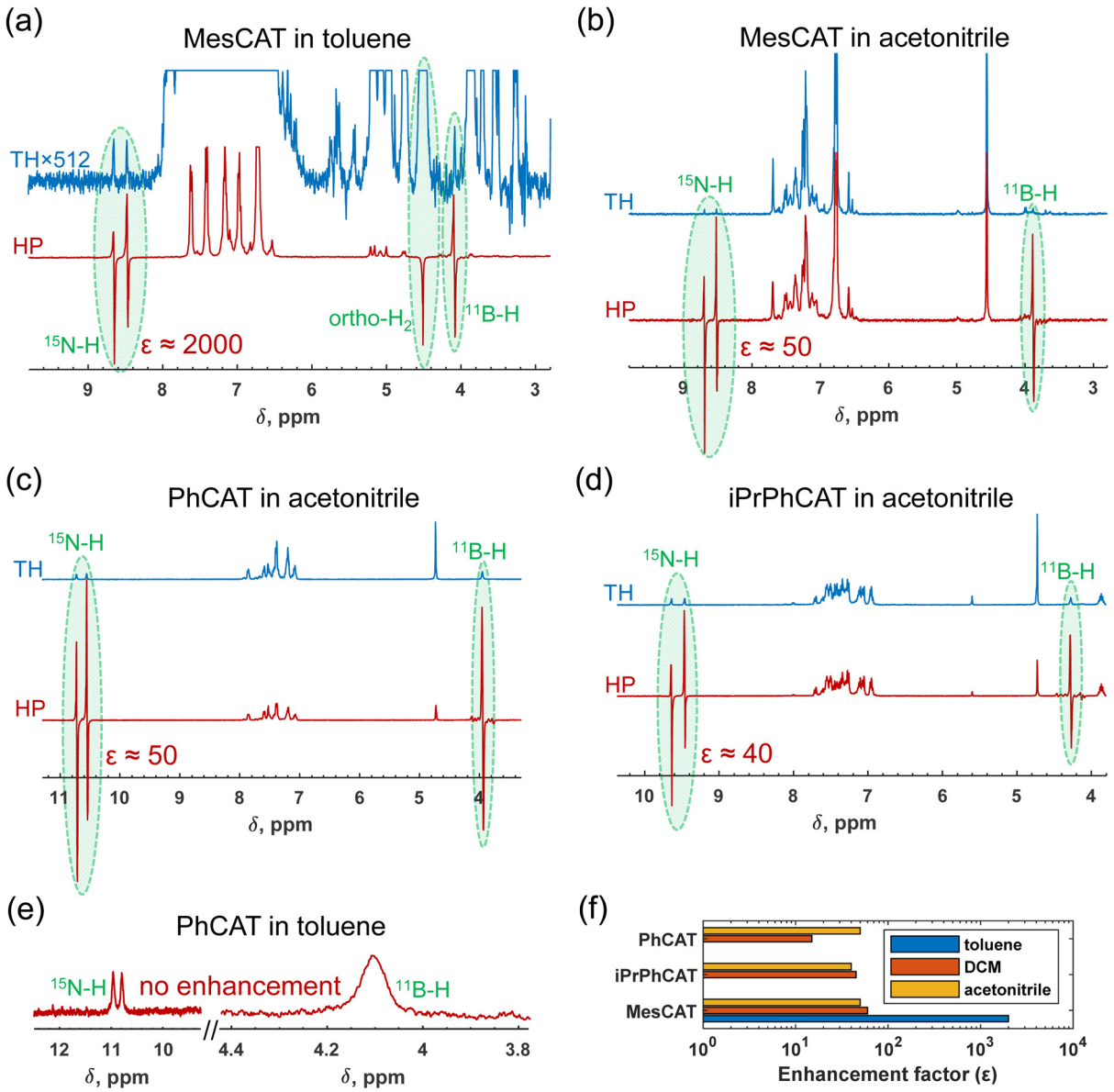

Fig. 4 ^{1}H {^{11}B} NMR spectra (a)–(e) measured after parahydrogen bubbling through 0.05 M solutions of the studied *ansa*-aminoboranes in various solvents and a histogram plot (f) illustrating NMR signal enhancements achieved in these experiments. The data corresponds to **MesCAT** in toluene-d_8 (a) and acetonitrile-d_3 (b), **PhCAT** in toluene-d_8 (e) and acetonitrile-d_3 (c), as well as **iPrPhCAT** in acetonitrile-d_3 (d). The signal enhancement factors, ε, are shown in the figure for the relevant cases when enhanced antiphase signals of parahydrogen-originating protons were observed. Thermal signals are also presented for comparison. TH = thermal, HP = hyperpolarized.

 This journal is © the Owner Societies 2024

Open Access Article. Published on 22 December 2023. Downloaded on 5/7/2026 11:03:45 AM.
This article is licensed under a Creative Commons Attribution 3.0 Unported Licence.

to the stabilization effect of dihydrogen bonding in the AAB-H_2 adducts.[4] The rotamers in which the borohydride groups are rotated by 120° (**Rot**$^-$ and **Rot**$^+$ forms) are predicted to be 5–6 kcal mol^{-1} higher for **PhCAT-H$_2$** and **MesCAT-H$_2$**. In the **Rot**$^-$ form of **iPrPhCAT-H$_2$**, the steric hindrance is enhanced, resulting in a less favoured structure lying at 8 kcal mol^{-1} in free energy (see ESI,† for structures). Nevertheless, the rotation is actually feasible in all AAB-H_2 adducts, as the free energy barriers of rotations are notably lower than those of the corresponding adduct dissociation processes, and therefore they allow for fast intramolecular structural rearrangements on the time scale of dissociation.

The barrier of the rotation is predicted to be lowest for **PhCAT-H$_2$** (8.7 kcal mol^{-1}), but it becomes significantly higher with **MesCAT-H$_2$** (15.1 kcal mol^{-1}). The destabilization of the related transition states **Rot**$^-$**-TS** and **Rot**$^+$**-TS** is evidenced by the distorted mesityl units of these structures (see ESI†). Although $BHAr_2$ rotation appears to be feasible kinetically, the relative stabilities computed for the rotated structures of AAB-H_2 (5–8 kcal mol^{-1}) suggest a very low population of these states (<1% at room temperature).

3.3 Parahydrogen experiments

Based on observations, the use of parahydrogen as H_2 feedstock in the activation process with *ansa*-aminoboranes leads to nuclear spin hyperpolarization of AAB-H_2 species due to the dynamic chemical equilibrium characterized above. To demonstrate this effect in different solvents, we performed reference experiments by bubbling parahydrogen (92%, 5 bar) through 0.05 M solutions of *ansa*-aminoboranes (**MesCAT**, **iPrPhCAT**, **PhCAT**) in toluene-d_8 and acetonitrile-d_3 at room temperature, which culminated in the consequent acquisition of ^{1}H NMR spectra. π/4-pulses were used for the radio-frequency (RF) excitation to maximize signal amplitudes according to the PASADENA protocol for weakly coupled correlated spins.[33] Similar experiments utilizing dichloromethane as a solvent have been reported previously.[4] Fig. 4 provides an overview of how the hyperpolarization exhibits a strong dependence on the solvent used and the AAB structure.

Specifically, **MesCAT** showed antiphase doublets, indicating the formation of the hyperpolarized **MesCAT-H$_2$** adduct in both toluene and acetonitrile solvents (Fig. 1a and b). In contrast, **iPrPhCAT** and **PhCAT** demonstrated the formation of corresponding hyperpolarized adducts with parahydrogen only in acetonitrile (Fig. 1c and d). Signals of only thermally polarized species were observed in toluene for these *ansa*-aminoboranes. Interestingly, all AABs showed some degree of hyperpolarization in dichloromethane-d_2, as was reported previously in ref. 4.

Measured signal enhancements reveal an ambiguous trend with respect to the solvent and *ansa*-aminoborane used. For instance, the summarizing histogram in Fig. 1f shows that as high as 2000-fold signal enhancement was observed in toluene in the case of **MesCAT**, whereas it was 50-fold in the case of acetonitrile. In contrast, the reaction with **PhCAT** in toluene resulted in the absence of signal enhancement (no hyperpolarization), whereas

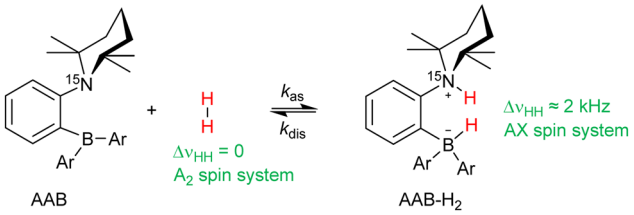

Scheme 2 Activation of molecular hydrogen by *ansa*-aminoboranes.

in acetonitrile, AAB-H_2 signals were again enhanced by a factor of 50.

As presented in Section 3.1, the kinetic and thermodynamic parameters of H_2 activation (k_{as}, k_{dis}, K_c) also reveal significant differences between the solvents (Table 1). It is obvious that the observed hyperpolarization effects are dependent on those parameters, and this is the origin of the solvent dependence of the hyperpolarization. To elaborate on this implication in more detail, the processes leading to hyperpolarization can be understood as follows: during parahydrogen bubbling through the solutions of *ansa*-aminoboranes, the reversible chemical activation of H_2 leads to the accumulation of a non-equilibrium nuclear spin order in the corresponding hydrogen adduct molecules (Scheme 2). To understand the general features of the resulting hyperpolarization, as a first approximation, it is sufficient to consider only a pair of parahydrogen originating hydrogen nuclei in the adduct molecules, neglecting long-range spin–spin couplings to any other protons as they are small.

Parahydrogen is a source of singlet nuclear spin order:[13]

$$\hat{\rho}_p = \frac{\hat{E}}{4} - \hat{I}_{1x}\hat{I}_{2x} - \hat{I}_{1y}\hat{I}_{2y} - \hat{I}_{1z}\hat{I}_{2z}. \quad (1)$$

At the same time, it is good to note that zero-quantum coherence ($\hat{I}_{1x}\hat{I}_{2x} + \hat{I}_{1y}\hat{I}_{2y}$) and longitudinal two-spin order ($\hat{I}_{1z}\hat{I}_{2z}$) are not coupled by the isotropic spin Hamiltonian in neither H_2 nor in AAB-H_2 molecules,[4] meaning that to get general ideas about observed hyperpolarization effects, the evolution of these orders in the reaction process can be considered separately. Due to the significant chemical shift difference (≈2 kHz) of the parahydrogen nascent ^{1}H nuclei in AAB-H_2 adducts and the relatively small *J*-coupling between them (≈3 Hz),[4] zero-quantum coherence will vanish in the adducts due to kinetic averaging, hence contributing negligibly to the density operator. In contrast, the longitudinal nuclear spin order will be preserved since it commutes with the isotropic spin Hamiltonian. This brings a significant simplification to the formal description of the process, as kinetic equations can be basically reduced to a simplified effective nuclear spin order:[33,34]

$$\hat{\rho}_e = \frac{\hat{E}}{4} - \hat{I}_{1z}\hat{I}_{2z}. \quad (2)$$

This nuclear spin order in particular leads to the observation of enhanced antiphase signals of parahydrogen-originating protons after application of radio-frequency pulses in Fig. 4 (see Section 1.2.2 in ESI,† for details).[33] Therefore, it is important to look into the accumulation of $\hat{\rho}_e$ in the H_2 and AAB-H_2 pools

Open Access Article. Published on 22 December 2023. Downloaded on 5/7/2026 11:03:45 AM.
This article is licensed under a Creative Commons Attribution 3.0 Unported Licence.

during parahydrogen bubbling. Assuming the thermodynamic chemical equilibrium in Scheme 1, the formal kinetic equations describing this process can be read as

$$\frac{d\langle\hat{\rho}_e\rangle_f}{dt} = k_0\langle\hat{\rho}_e\rangle_0 - k_{as}[AAB]_0\langle\hat{\rho}_e\rangle_f - {T_{1f}}^{-1}\langle\hat{\rho}_e\rangle_f + k_{dis}\langle\hat{\rho}_e\rangle_b - k_0\langle\hat{\rho}_e\rangle_f, \quad (3)$$

$$\frac{d\langle\hat{\rho}_e\rangle_b}{dt} = k_{as}[AAB]_0\langle\hat{\rho}_e\rangle_f - k_{dis}\langle\hat{\rho}_e\rangle_b - {T_{1b}}^{-1}\langle\hat{\rho}_e\rangle_b, \quad (4)$$

where $k_0\langle\hat{\rho}_e\rangle_0$ is the rate of $\hat{\rho}_e$ supply induced by parahydrogen bubbling through AAB solutions, whereas T_{1f} and T_{1b} are the relaxation times of this spin order in the forms of free H_2 and bound H_2 in AAB-H_2, respectively. To a good approximation, the relaxation in the free form can be neglected since it is much slower as compared to that in the bound form. If the lifetime of AAB-H_2 species is comparable with T_{1b}, the relaxation will significantly decrease $\langle\hat{\rho}_e\rangle_b$. At the same time, if the association of AAB and parahydrogen defined by $k_{as}[AAB]_0$ is fast, then the fast relaxation in the bound form will also noticeably destroy $\langle\hat{\rho}_e\rangle_f$ – the non-equilibrium spin order in the free species. Generally, kinetics and relaxation have a complex influence on the amplitude of generated $\langle\hat{\rho}_e\rangle_b$ and $\langle\hat{\rho}_e\rangle_f$. For instance, after a long enough time of parahydrogen bubbling through AAB solutions, a stationary state will be reached in which, according to eqn (3) and (4), theoretically achieved fractions of $\hat{\rho}_e$ in H_2 (ε_f) and AAB-H_2 (ε_b) pools have the following functional dependencies, respectively,

$$\varepsilon_f = \frac{1}{\frac{1}{k_0/k_{dis} + T_{1b}k_0}\cdot\xi + \frac{1}{T_{1f}k_0} + 1} \quad (5)$$

and

$$\varepsilon_b = \frac{1}{\frac{1}{T_{1b}k_0}\cdot\xi + \left(\frac{1}{T_{1b}k_{dis}} + 1\right)\left(\frac{1}{T_{1f}k_0} + 1\right)}, \quad (6)$$

where

$$\xi = \frac{k_{as}[AAB]_0}{k_{dis}} = \frac{[AAB\text{-}H_2]_0}{[H_2]_0} = \frac{[AAB]_\Sigma}{[H_2]_0 + \frac{1}{K_c}} \quad (7)$$

is a concentration factor, $[AAB]_\Sigma = [AAB]_0 + [AAB\text{-}H_2]_0$ is the initial concentration of *ansa*-aminoborane before the reaction, and K_c is the equilibrium constant. Note that in the limit of fast parahydrogen saturation (large k_0), ε_b has the form derived in our previous report, see eqn (3) in ref. 4. In addition, if K_c is big (a lot of AAB-H_2), then the enhancement becomes strongly dependent on the concentration of H_2, whereas when K_c is small, then it is effectively independent from the concentration of H_2. Therefore, the solubility of H_2 can be one of the important factors for the hyperpolarization.

The time evolution before reaching the stationary state and after interruption of parahydrogen bubbling is a complex process reflecting the interplay between mass transport of parahydrogen, the kinetics and thermodynamics of H_2 activation, and the relaxation processes leading to the decay of the non-equilibrium nuclear spin order. It is difficult to find simple analytical expressions describing these transient processes. The numerical solutions presented in Fig. 5 illustrate the basic features of accumulation and decay of the longitudinal two spin order ($\hat{\rho}_e$, eqn (2)) for **PhCAT** and **MesCAT** in toluene based on the corresponding experimental kinetic and thermodynamic parameters from Table 1. The stationary state for $\hat{\rho}_e$ is reached after *ca.* 2 and 10 s for **PhCAT** (Fig. 5a) and **MesCAT** (Fig. 5b), respectively. The concentration normalized amplitudes ($\hat{\rho}_e/[C]$), however, differ by an order of magnitude, indicating much weaker stationary hyperpolarization in the case of **PhCAT**. This state is preserved for both H_2 and AAB-H_2 pools until the moment when the parahydrogen supply is stopped at t = 25 s. After this point, the accumulated non-equilibrium order starts to decay to zero, thus it is important to apply the read π/4-pulse

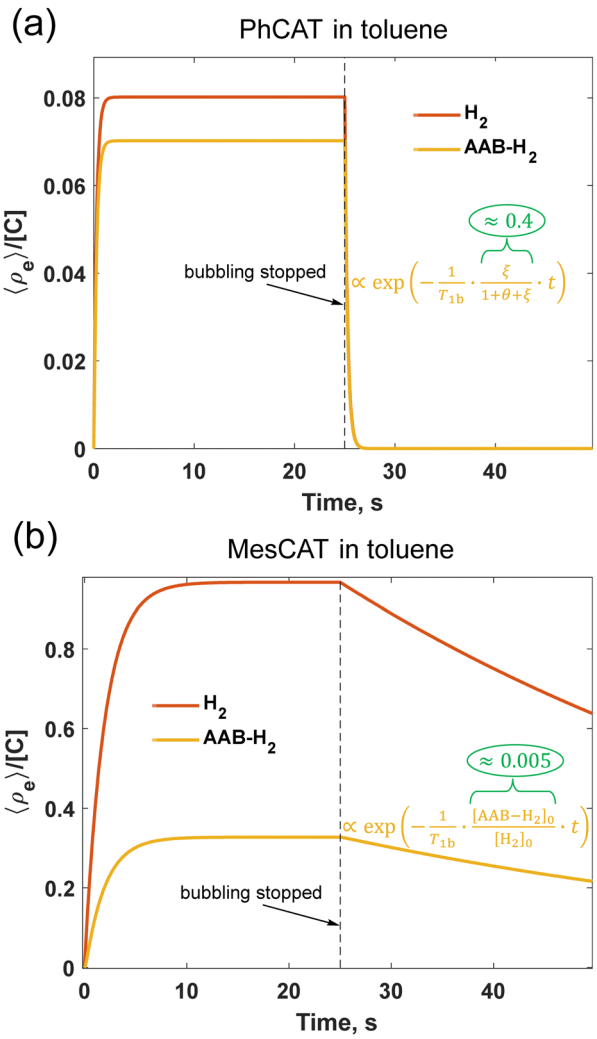

Fig. 5 Dynamics of the longitudinal nuclear spin order in 0.05 M solutions of **PhCAT** (a) and **MesCAT** (b) at 298 K in toluene-d_8 according to the kinetic model described by eqn (3) and (4) with experimentally measured reaction rate parameters of Table 1. The first half of the graphs illustrates accumulation (“pumping”) of the spin order during the parahydrogen bubbling, and the second half correspond to the decay of the order after the parahydrogen supply was stopped (see ESI,† for details of the modelling; $\theta = 1/k_{dis}T_{1b}$).

This journal is © the Owner Societies 2024

Open Access Article. Published on 22 December 2023. Downloaded on 5/7/2026 11:03:45 AM.
This article is licensed under a Creative Commons Attribution 3.0 Unported Licence.

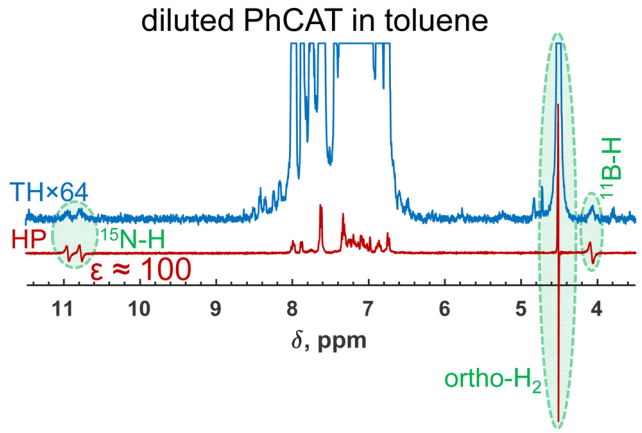

Fig. 6 ^{1}H NMR spectra measured after parahydrogen bubbling through a 0.001 M solution of **PhCAT** that demonstrate the observation of strongly enhanced antiphase doublets of the parahydrogen-originating protons of **PhCAT-H$_2$**. Note that the 50 times more concentrated solution did not result in any hyperpolarization effects (see Fig. 2e), clearly illustrating the influence of the concentration factor. Additionally, a partially negative line effect is observed for the orthohydrogen resonance.

and detect the signal as soon as possible after parahydrogen supply (*e.g.*, bubbling) is stopped. Importantly, in the case of **PhCAT**, this decay is very fast, leading to 95% of the spin order drop after 1 s (Fig. 5a). Both the low stationary level and fast decay of the spin order result in the absence of hyperpolarization effects for **PhCAT** in toluene (Fig. 4e). In contrast, the situation is significantly more favorable in the case of **MesCAT** (Fig. 5b), since both the higher stationary spin order amplitude and the relatively slow decay should result in strong hyperpolarization effects observed experimentally (Fig. 4a).

It is worth noting that this discussion primarily concerns the AAB-H$_2$ pool since the hyperpolarization is revealed when the parahydrogen-originating protons are inequivalent (AX spin system). Indeed, the accumulated longitudinal two-spin order in the free H$_2$ hydrogen pool, $\langle\hat{\rho}_e\rangle_f$, to a first approximation, is not observable by $\pi/4$-pulse pulse method in the same way as for AAB-H$_2$, since the antiphase transverse magnetization does not evolve into its observable in-phase counterpart due to the equality of the observed Larmor frequencies of nuclei, *i.e.*, strong coupling. If the frequencies are equal, the density operator derived from $\hat{I}_{1x}\hat{I}_{2z} + \hat{I}_{1z}\hat{I}_{2x}$ always commutes with the scalar term in the spin Hamiltonian during the time evolution. However, some subtle effects, such as the partially negative line (PNL) effect for orthohydrogen, can reveal specific manifestations of the generated non-equilibrium order.[4,35] Effectively, this happens due to the fact that chemical exchange can slightly alter the observed resonance frequencies, breaking the symmetry of the isotropic spin Hamiltonian. In addition, cross-correlated relaxation can transform the longitudinal two-spin order of $\hat{\rho}_e$ into single spin longitudinal magnetization in some cases, which leads to the enhanced in-phase negative magnetization of orthohydrogen (see, for instance, Fig. 1a).[4–7] Both of these effects are observable in experiments with *ansa*-aminoboranes, but they are typically minor, and their description is much more complicated to analyze precisely. Therefore, we focus on the antiphase magnetization in AAB-H$_2$, the major hyperpolarization effect, to characterize different *ansa*-aminoboranes in different solvents.

Based on the known experimental kinetic and relaxation parameters (Table 1), we can model the response of the nuclear spin order buildup on an alternation of experimental conditions to optimize the observed hyperpolarization signals. For instance, the absence of hyperpolarization in the case of the 0.05 M solution of **PhCAT** in toluene is probably the clearest example of suboptimal conditions for the hyperpolarization. In spite of the fact that the kinetics of the reaction is fast in both directions, the enhanced signals were not observed since the nuclear spin relaxation effectively destroys the hyperpolarization due to the rapid formation of a large rapidly relaxing **PhCAT-H$_2$** pool. This makes a clear difference with **MesCAT**, for which the **MesCAT-H$_2$** pool is two orders of magnitude smaller than the slowly relaxing H$_2$ pool (see $[\text{AAB-H}_2]_0/[\text{H}_2]_0$ ratios in Table 1). This implies that the size variation of these pools can influence the observed polarization level. Note that eqn (6) explicitly includes concentration factor (eqn (7)) dependence, which we can vary in experiments.

Indeed, when we used a diluted sample with a decreased concentration of **PhCAT** by 50 times in toluene while keeping the other parameters and the parahydrogen pressure at the same level, strong hyperpolarization was detected (Fig. 6). From the no enhancement, the dilution led to a 100-fold amplification of the parahydrogen-originating protons in **PhCAT-H$_2$** (see antiphase NH and BH signals). Of course, one needs to keep in mind that this was done at the price of decreased amplitudes of the thermal signals, but this can be beneficial in certain situations, for instance, when it is not preferable to use concentrated samples. Overall, this experiment demonstrated that knowledge of the reaction kinetics and mechanism can provide freedom in selecting one or another *ansa*-aminoborane for PHIP experiments.

4. Conclusions

Ansa-aminoboranes can provide interesting capabilities for the activation of molecular hydrogen and, generally, for hydrogenation catalysis without metals. Characterization of the mechanistic details of the activation can be very helpful in designing highly efficient metal-free catalysts. In this study, we consider this process on both macroscopic and microscopic levels. Utilizing these data, we rationalize experimental observations of nuclear spin hyperpolarization effects in different solvents when parahydrogen was used as H$_2$ feedstock. We show that the presented vast amount of experimentally measured kinetic and thermodynamic parameters for **MesCAT**, **iPrPhCAT**, and **PhCAT** *ansa*-aminoboranes can be employed to find optimal conditions for the observation of strong spin hyperpolarization. The discussed microscopic picture of the activation process shows the active dynamics around the FLP centers, such as inversion of the TMP ring and rotation of the

Open Access Article. Published on 22 December 2023. Downloaded on 5/7/2026 11:03:45 AM.
This article is licensed under a Creative Commons Attribution 3.0 Unported Licence.

boryl site. Nevertheless, our DFT calculations reveal that the most stable forms of H_2 adducts are those where the two hydrogen atoms are in close proximity to each other, which is attributed to the stabilization effect of dihydrogen bonding. Moreover, it is shown experimentally and computationally that the polarity of the solvent is an important factor that shifts the chemical equilibrium towards the formation of H_2 adducts and decreases the adduct dissociation rate. It is demonstrated that the computed thermochemical parameters match the experimentally measured ones to a good accuracy level, opening an avenue for extensive modelling of molecular metal-free catalysts for parahydrogen-induced polarization studies. Altogether, this gives a solid foundation for further rational design of efficient metal-free catalytic systems for NMR sensitivity enhancement and NMR sensing applications based on *ansa*-aminoboranes.

Author contributions

K. K.: investigation, validation, writing – review and editing; G. L.: investigation, validation, visualization, writing – review and editing; I. P.: conceptualization, funding acquisition, resources, supervision, validation, writing – review and editing; V. V. Z.: conceptualization, funding acquisition, resources, supervision, validation, visualization, writing – original draft.

Conflicts of interest

There are no conflicts to declare.

Acknowledgements

We are grateful for the support of this work by the Academy of Finland (grant no. 323480) and the University of Oulu (Kvantum Institute). Financial support from the National Research, Development, and Innovation Office (NKFIH) is gratefully acknowledged (grant K-142486). We thank Dr Konstantin Chernichenko, Dr Kristina Sorochkina and Prof. Timo Repo from the University of Helsinki for their assistance with the synthesis of *ansa*-aminoborane samples for the experiments. V. V. Z. wishes to acknowledge CSC – IT Center for Science, Finland, for computational resources (CSC project 2004016).

Notes and references

1 J. Lam, K. M. Szkop, E. Mosaferi and D. W. Stephan, *Chem. Soc. Rev.*, 2019, **48**, 3592–3612.
2 A. R. Jupp and D. W. Stephan, *Trends Chem.*, 2019, **1**, 35–48.
3 V. V. Zhivonitko, V.-V. Telkki, K. Chernichenko, T. Repo, M. Leskelä, V. Sumerin and I. V. Koptyug, *J. Am. Chem. Soc.*, 2014, **136**, 598–601.
4 V. V. Zhivonitko, K. Sorochkina, K. Chernichenko, B. Kotai, T. Földes, I. Pápai, V.-V. Telkki, T. Repo and I. Koptyug, *Phys. Chem. Chem. Phys.*, 2016, **18**, 27784–27795.
5 K. Sorochkina, V. V. Zhivonitko, K. Chernichenko, V. V. Telkki, T. Repo and I. V. Koptyug, *J. Phys. Chem. Lett.*, 2018, **9**, 903–907.
6 D. O. Zakharov, K. Chernichenko, K. Sorochkina, S. Yang, V. V. Telkki, T. Repo and V. V. Zhivonitko, *Chem. – Eur. J.*, 2022, **28**, e202103501.
7 D. O. Zakharov, K. Chernichenko, K. Sorochkina, T. Repo and V. V. Zhivonitko, *Dalton Trans.*, 2022, **51**, 13606–13611.
8 B. J. Tickner and V. V. Zhivonitko, *Chem. Sci.*, 2022, **13**, 4670–4696.
9 L. E. Longobardi, C. A. Russell, M. Green, N. S. Townsend, K. Wang, A. J. Holmes, S. B. Duckett, J. E. McGrady and D. W. Stephan, *J. Am. Chem. Soc.*, 2014, **136**, 13453–13457.
10 V. V. Zhivonitko, J. Bresien, A. Schulz and I. V. Koptyug, *Phys. Chem. Chem. Phys.*, 2019, **21**, 5890–5893.
11 V. V. Zhivonitko, H. Beer, D. O. Zakharov, J. Bresien and A. Schulz, *ChemPhysChem*, 2021, **22**, 813–817.
12 E. Zander, J. Bresien, V. V. Zhivonitko, J. Fessler, A. Villinger, D. Michalik and A. Schulz, *J. Am. Chem. Soc.*, 2023, **145**, 14484–14497.
13 C. R. Bowers and D. P. Weitekamp, *Phys. Rev. Lett.*, 1986, **57**, 2645–2648.
14 C. R. Bowers and D. P. Weitekamp, *J. Am. Chem. Soc.*, 1987, **109**, 5541–5542.
15 S. B. Duckett and N. J. Wood, *Coord. Chem. Rev.*, 2008, **252**, 2278–2291.
16 B. Procacci, P. M. Aguiar, M. E. Halse, R. N. Perutz and S. B. Duckett, *Chem. Sci.*, 2016, **7**, 7087–7093.
17 R. Giernoth, P. Huebler and J. Bargon, *Angew. Chem., Int. Ed.*, 1998, **37**, 2473–2475.
18 S. Aime, W. Dastru, R. Gobetto, F. Reineri, A. Russo and A. Viale, *Organometallics*, 2001, **20**, 2924–2927.
19 C. J. Sleigh, S. B. Duckett and B. A. Messerle, *Chem. Commun.*, 1996, 2395–2396.
20 S. B. Duckett, in *Encyclopedia of Spectroscopy and Spectrometry*, ed. J. C. Lindon, G. E. Tranter and D. W. Koppenaal, Elsevier, 3rd edn, 2016, pp. 527–534, DOI: 10.1016/B978-0-12-409547-2.12126-2.
21 K. V. Kovtunov, O. G. Salnikov, V. V. Zhivonitko, I. V. Skovpin, V. I. Bukhtiyarov and I. V. Koptyug, *Top. Catal.*, 2016, **59**, 1686–1699.
22 K. V. Kovtunov, V. V. Zhivonitko, I. V. Skovpin, D. A. Barskiy and I. V. Koptyug, *Top. Curr. Chem.*, 2013, **338**, 123–180, DOI: 10.1007/128_2012_371.
23 R. L. Jarek, R. J. Flesher and S. K. Shin, *J. Chem. Educ.*, 1997, **74**, 978.
24 M. Montag, J. Zhang and D. Milstein, *J. Am. Chem. Soc.*, 2012, **134**, 10325–10328.
25 W. G. Wang, T. B. Rauchfuss, L. Y. Zhu and G. Zampella, *J. Am. Chem. Soc.*, 2014, **136**, 5773–5782.
26 P. W. Atkins and J. De Paula, in *Physical chemistry*, W. H. Freeman, Oxford University Press, Peter Atkins, Julio de Paula, New York, Oxford, 9th edn, 2010.
27 J. D. Chai and M. Head-Gordon, *Phys. Chem. Chem. Phys.*, 2008, **10**, 6615–6620.
28 J. D. Chai and M. Head-Gordon, *J. Chem. Phys.*, 2008, **128**, 084106.
29 S. Grimme, *J. Comput. Chem.*, 2006, **27**, 1787–1799.

 This journal is © the Owner Societies 2024

Open Access Article. Published on 22 December 2023. Downloaded on 5/7/2026 11:03:45 AM.
This article is licensed under a Creative Commons Attribution 3.0 Unported Licence.

30 A. V. Marenich, C. J. Cramer and D. G. Truhlar, *J. Phys. Chem. B*, 2009, **113**, 6378–6396.
31 M. J. Frisch, G. W. Trucks, H. B. Schlegel, G. E. Scuseria, M. A. Robb, J. R. Cheeseman, G. Scalmani, V. Barone, G. A. Petersson, H. Nakatsuji, X. Li, M. Caricato, A. V. Marenich, J. Bloino, B. G. Janesko, R. Gomperts, B. Mennucci, H. P. Hratchian, J. V. Ortiz, A. F. Izmaylov, J. L. Sonnenberg, D. Williams-Young, F. Ding, F. Lipparini, F. Egidi, J. Goings, B. Peng, A. Petrone, T. Henderson, D. Ranasinghe, V. G. Zakrzewski, J. Gao, N. Rega, G. Zheng, W. Liang, M. Hada, M. Ehara, K. Toyota, R. Fukuda, J. Hasegawa, M. Ishida, T. Nakajima, Y. Honda, O. Kitao, H. Nakai, T. Vreven, K. Throssell, J. A. Montgomery Jr., J. E. Peralta, F. Ogliaro, M. J. Bearpark, J. J. Heyd, E. N. Brothers, K. N. Kudin, V. N. Staroverov, T. A. Keith, R. Kobayashi, J. Normand, K. Raghavachari, A. P. Rendell, J. C. Burant, S. S. Iyengar, J. Tomasi, M. Cossi, J. M. Millam, M. Klene, C. Adamo, R. Cammi, J. W. Ochterski, R. L. Martin, K. Morokuma, O. Farkas, J. B. Foresman and D. J. Fox, *Gaussian 16 Rev. E.01*, Wallingford CT, 2016.
32 T. A. Rokob, I. Bako, A. Stirling, A. Hamza and I. Pápai, *J. Am. Chem. Soc.*, 2013, **135**, 4425–4437.
33 C. R. Bowers, in *Encyclopedia of Nuclear Magnetic Resonance*, ed. D. M. Grant and R. K. Harris, Wiley, Chichester, 2002, vol. 9, pp. 750–769.
34 J. Natterer and J. Bargon, *Prog. Nucl. Magn. Reson. Spectrosc.*, 1997, **31**, 293–315.
35 A. S. Kiryutin, G. Sauer, A. V. Yurkovskaya, H. H. Limbach, K. L. Ivanov and G. Buntkowsky, *J. Phys. Chem. C*, 2017, **121**, 9879–9888.